JOURNAL OF MATERIALS SCIENCE 30 (1995) 4249–4262

In situ strengthening of titanium with yttrium: texture analysis

A. M. RUSSELL, L. S. CHUMBLEY, T. W. ELLIS, F. C. LAABS
Ames Laboratory, Iowa State University, Ames, IA 50011, USA

B. NORRIS
Rohr, Inc., Chula Vista, CA 92012, USA

G. E. DONIZETTI
G & S Titanium, Wooster, OH 44691, USA

In situ processing consists of heavily deforming a two-phase alloy of mutually immiscible elements to produce composite sheet or wire. In the well-studied Cu(fcc)–Nb(bcc) system, severe deformation by swaging and drawing reduces as-cast Nb filament phase thicknesses several hundred-fold after deformation. Cu–20 vol% Nb ultimate tensile strengths exceed 2000 MPa for material deformed to a true strain of $\eta = 12$, where $\eta = \ln(\text{area}_{\text{original}}/\text{area}_{\text{final}})$.

In an earlier study of *in situ* strengthening in immiscible hexagonal close-packed metals, Ti–50 vol% Y and Ti–20 vol% Y alloys were deformed by hot extrusion, hot and cold swaging. The composites were deformation processed to true strains as high as $\eta = 7.6$ to form a filamentary microstructure with filament thicknesses on the order of 0.1 μm. The deformation processing of these composites increased their ultimate tensile strengths from 318 to 945 MPa, but the specimens' original diameters were too small to allow deformation processing to the very high true strains achieved with the Cu–Nb composites.

In this study, a larger casting of Ti–20 vol% Y was deformation processed to $\eta = 12.8$ in an attempt to achieve further refinement of the filament thickness. This composite formed the same filamentary microstructure up to $\eta = 7.27$ observed in the earlier study of Ti–Y composites; however, at higher η values the filaments recrystallized into equiaxed grains, decreasing the ultimate tensile strength. X-ray texture analysis of the composite specimens showed a strong $\langle 10\bar{1}0 \rangle$ fibre texture in both the Ti and Y phases in the deformation processing range $2.25 \leq \eta \leq 7.27$. This texturing is thought to constrain both the Ti and Y phases to deform by plane strain, which produces severe geometric restrictions on the ability of the plane straining filaments to achieve high η values without fracturing or recrystallizing.

1. Introduction

1.1. *In situ* composite Cu–X alloys

During the past several years, a new class of copper-refractory metal alloys (Cu–X) has been developed with extraordinary mechanical and electrical properties [1–3]. These alloys, comprised of Cu(fcc) with 10–30% element X (where X is a bcc metal immiscible in Cu such as Nb, V, Ta, Cr or Fe), are severely deformed to produce a nanometre-scale microstructure of X filaments (when deformed by drawing) or lamellae (by rolling) in the Cu matrix. The Cu–20% Nb system is the most thoroughly studied of these alloys and has ultimate tensile strengths exceeding 2000 MPa after deformation to a true strain of $\eta = 12$ [where $\eta = \ln$(initial cross-sectional area/final cross sectional area)] [4].

The Cu–X alloys are characterized by remarkable ductility, which allows cast or powder processed starting billets to be deformed to as much as $\eta = 13.4$ before breaking [5]. Such deformations represent more than an 800-fold reduction in diameter and are accompanied by a concomitant reduction in the thickness and spacing of the Cu and X phases. Thus, an as-cast billet of Cu–20 vol% Nb, displaying Nb dendrites of average thickness 4 μm, may be deformation processed at room temperature into a wire with Nb filaments averaging 7 nm thick [6]. Such *in situ* processed composite alloys have strengths substantially higher than those of any other Cu alloy. Debate continues on the mechanism(s) which account for the very high strengths of the Cu–X alloys [7–11], but discussion centres around the role of the nanofilamentary X structure in impeding propagation and motion of dislocations in both the Cu and X phases.

1.2. *In situ* composite Ti alloys

A preliminary investigation by Russell *et al.* [12] of the deformation processing behaviour of an hcp–hcp Ti–Y composite was performed in the hope that

0022–2461

a non-cubic deformation-processed composite might provide insights into the fundamental mechanism(s) of *in situ* strengthening. In addition, if strengths comparable to those seen in the Cu-matrix composites could be achieved in the Ti–Y system, a potentially useful low density, high strength composite might result.

In that preliminary study, Ti–50 vol % Y and Ti–20 vol % Y composites were deformation processed to true strains of $\eta = 6.6$ and 7.6, respectively. Both compositions were deformed by hot extrusion and swaging at 725–860 °C, followed by room temperature swaging with 615 °C recovery anneals *in vacuo* after each 20% reduction in area. This processing produced a microstructure of long, ribbon-shaped filaments of Ti and Y which became progressively thinner as the deformation progressed. The finest filaments produced were 0.1 μm thick in the Ti–20 vol % Y composite at $\eta = 7.6$, and the ultimate tensile strength of the Ti–20 vol % Y increased three-fold from 318 (as-cast) to 945 MPa at $\eta = 7.6$. Unfortunately, the specimens' original diameters were too small to allow deformation processing to the very high true strains achieved with the Cu–Nb composites.

2. Experimental procedures

2.1. Alloy preparation and deformation

Shortly after conclusion of that first study of Ti–Y composites, a second study began with a larger diameter (74 mm) arc-melted casting of Ti–20 vol % Y (hereinafter referred to as Ti–20Y). The Ti used for this casting was 99.9% pure (210 wt p.p.m. O), and the Y was 99.8% pure (976 wt p.p.m. O). This specimen and an accompanying 74 mm diameter control specimen of pure Ti cast from the same Ti stock were welded into an evacuated steel can and extruded at 800°C through a 3:1 reducing die ($\eta = 2.25$) . The extruded specimens, still within steel outer sleeves, were then swaged at room temperature. Swaging was performed in stages with a 60% reduction in cross-sectional area by swaging followed by a 30 min stress-relief anneal in air at 700 °C; this was, in turn, followed by another 60% reduction and another stress-relief anneal at 700 °C, and so forth, until the specimens had been reduced to a 2.5 mm diameter ($\eta = 6.8$) .

At a diameter of 2.5 mm, both specimens were placed in a H_2SO_4 acid bath to etch away the steel jackets and expose the Ti–20Y and pure Ti. The deformation processing of the pure Ti was stopped at this point, and the Ti–20Y composite was deformed further by room temperature drawing in dies with an 8° taper reducing the diameter by 20% in each pass. The wire drawing followed the same precept used in swaging: 60% reduction in area, followed by a 30 min anneal in an inert atmosphere at 700 °C, repeated several times until the specimens reached a final diameter of 0.127 mm ($\eta = 12.8$).

A different deformation process was performed on a portion of the Ti–20Y composite and a portion of the pure Ti control specimen. These specimens (hereinafter referred to as "second generation" specimens) were removed from the deformation process described above at $\eta = 5.03$ and hot swaged at 700 °C to $\eta = 5.71$. Still encased in their steel jackets, these specimens were then swaged at room temperature to $\eta = 10.0$ with periodic 20 min anneals at 600 °C after each 25% reduction in cross-sectional area.

Coupons were removed from the specimens at several intermediate diameters for tensile testing, SEM and TEM examination of the microstructure, gas fusion analysis, and X-ray texture analysis.

2.2. Tensile testing procedures and ductility measurements

Tensile testing procedures for specimens in the range $\eta = 0$–9.2 followed ASTM Standard E8, which requires a 4:1 ratio between the length and the diameter of the specimen gauge length. In the as-cast tests, specimens were cut radially from the upper surface of the Ti–20Y casting and from the lower surface of the pure Ti casting. All other tensile test specimens were simply machined in a lathe around the cylindrical specimen axis until ASTM E8 geometry was attained. Specimen gauge lengths were polished with 500-mesh abrasive paper to eliminate lathe tool marks around the gauge length circumference. Specimens in the range $\eta = 0$–9.2 were tensile tested at a crosshead speed of 0.50 mm min^{-1}.

Specimens in the range $\eta = 9.2$–11 were wires of diameter 0.70–0.30 mm, and their small diameters made it impractical to machine them to the ASTM E8 geometry. The wires were fitted with soft Cu sleeves that slipped over the wire ends, leaving a gauge length of exposed specimen approximately four times the wire diameter between the copper sleeve ends. The Cu sleeves were cemented to the specimen wire ends, and the Cu was then forcefully compressed in a lathe collet while the cement was still wet to clamp it firmly around the specimen. Extremely light machining cuts were then made with a small rotating grinding stone (rather than a fixed cutting tool) on the rotating work piece to reduce the diameter of the specimen at the gauge length. During tensile testing, small pin vice grips were tightened around the Cu sleeves to apply the tensile load. For these smaller tensile specimens, a crosshead speed of 0.12 mm min^{-1} was applied.

The smallest tensile test specimens, where $\eta > 12$, were too fine to permit even the copper sleeve technique to be applied. Instead, a wire-pulling capstan device was used to apply the tensile load to an effective gauge length of 75 mm. This capstan device thus gave a much larger ratio of gauge length-to-diameter (600:1 for the 0.127 mm diameter wire of $\eta = 12.8$) than the 4:1 ratio specified in ASTM E8; however, no other means exist to provide tensile data on such fine wire. In this case, no attempt was made to reduce the diameter of the wire in the gauge length. Since tensile data are not critically sensitive to the length-to-diameter ratio of the specimen, it is believed that the capstan device still provides data approximately comparable to the data produced at the larger diameters, although the proportionally greater gauge length increases the possibility that an unrepresentatively low value of ultimate tensile strength may be produced due to the presence of an internal defect in the

specimen's gauge length. This possibility can be reduced by testing several specimens, and this was done to the extent that material was available. A crosshead speed of 0.25 mm min^{-1} was used with the capstan device tensile tests.

For all tensile tests, a value of engineering ultimate tensile strength was calculated from the quotient of the applied maximum load and the initial cross-sectional area of the specimen. Ductility was calculated for each specimen by measuring the area of the fracture surface in a travelling microscope and comparing that area to the original cross-sectional area of the specimen to calculate the per cent reduction in area.

2.3. Specimen preparation for SEM and TEM examination

SEM specimens were prepared by ordinary metallographic techniques and examined in an unetched condition. The large disparity in atomic number between Ti and Y provided strong contrast when using back-scattered electron imaging. A Cambridge S-200 microscope was used for all SEM photography.

For specimens of $\eta > 5.0$, TEM samples were used for measurements to avoid undercounting small phases that might lie beneath the resolving power of the SEM. TEM specimens were thinned by ion milling on a liquid nitrogen chilled stage. A Philips CM30 S/TEM operated at 300 kV was used for all TEM photography. Conical scan dynamic dark field imaging was used on many of the TEM micrographs to provide contrast between the Ti and Y phases.

For all pure Ti samples and for Ti–20Y samples without ribbon-shaped filaments, quantitative stereology [13] was used to measure mean free distance between grains or phases. In the Ti–20Y specimens possessing ribbon-shaped filaments ($2.25 \leq \eta \leq 7.27$), phase spacing determinations were made by measuring phase thicknesses across their short dimension and averaging these values.

2.4. Gas fusion analysis

The mechanical properties of Ti are sensitive to the presence of interstitial impurities (O, H, C and N) [14, 15]. Changes in the concentrations of these impurities amounting to only 0.1 wt % or less can substantially increase the strength and decrease the ductility of Ti. Consequently, analysis for O and N (the most likely of these interstitial solutes to contaminate the specimens from air leaks in vacuum systems) was conducted to assure that any strength increases observed were not caused by diffusion of O or N into the metals.

Gas fusion analysis specimens were cut from samples of both pure Ti and Ti–20Y deformation processed to $\eta = 0$ (as-cast), 2.25 (as-extruded) and 6.68. A sample of the Ti–20Y deformation processed to $\eta = 12.2$ was also analysed.

2.5. X-ray texture analysis

Transverse cross-section specimens were cut from both the pure Ti and the Ti–20Y composite at deformation levels of $\eta = 0$ (as-cast), 2.25 (as-extruded) and 5.03. A Ti–20Y texture specimen was also prepared at $\eta = 7.27$. Wire drawn to $\eta > 7.27$ were too fine to produce X-ray texture specimens. Each of the seven specimens was metallographically mounted and mechanically polished through a 1 μm diamond abrasive polish. The mechanically polished specimens were then electropolished in perchloric acid to remove the surface layer disturbed by mechanical polishing.

Pole figures were taken from the electropolished specimens with unfiltered molybdenum X-rays ($\lambda(K\alpha_{1\&2}) = 0.070930$ and 0.071359 nm and $\lambda(K\beta_1) = 0.063225$ nm). Data acquisition and analysis were performed by a Philips APD1700 Automated Powder Diffraction System. Each pole figure was acquired using a 5 mm sample lateral oscillation and a 5° per spiral φ (tilting) pitch. A 5 s sampling time was used with a 7.5° step in ϕ (rotation) between samplings. Measurements were made over the range $0° \leq \varphi \leq 80°$.

3. Results

3.1. The effect of deformation on microstructure

The Ti–20Y composite displayed progressively finer microstructure with increasing amounts of deformation. The as-cast microstructure was characteristic of two immiscible metals (Fig. 1). Initial hot work changed the original dendritic structure to a filamentary structure similar to that observed in Cu–X *in situ*

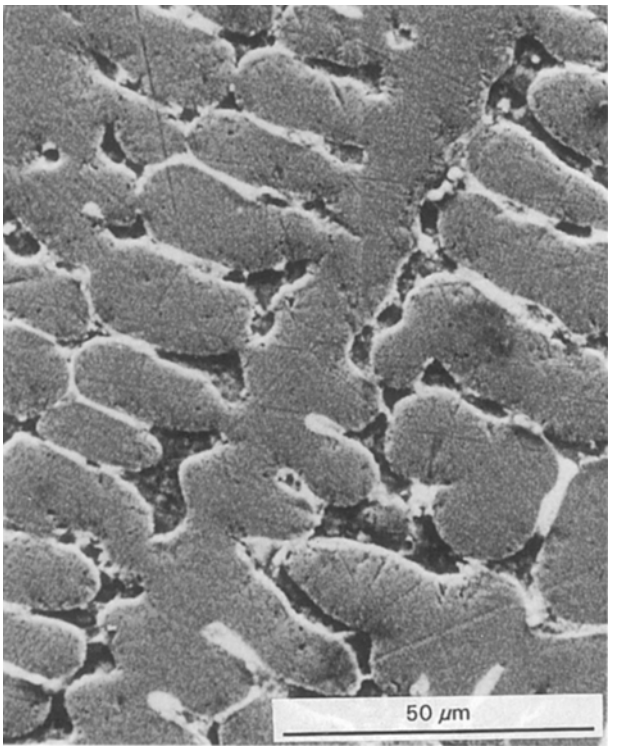

Figure 1 SEM back-scattered electron micrograph of as-cast Ti–20Y. The dark phase is Ti; the light phase is Y (pitted in places by the polishing agents).

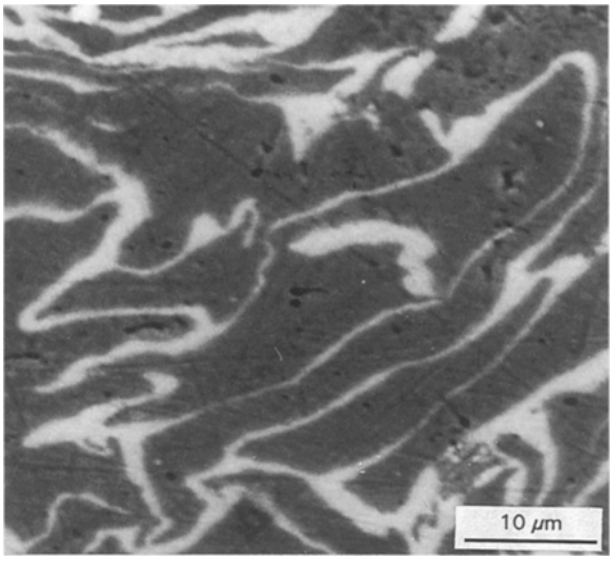

Figure 2 SEM back-scattered electron micrograph of a transverse section of Ti–20Y extruded at 800°C to $\eta = 2.25$. Dark grey areas are Ti; light grey areas are Y.

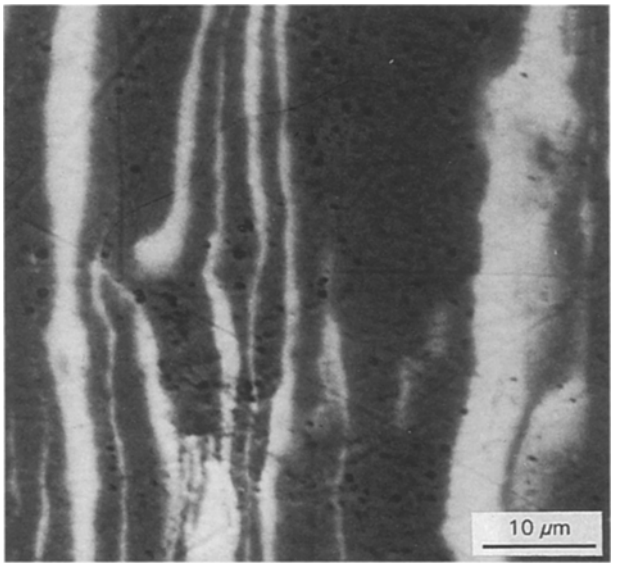

Figure 3 SEM back-scattered electron micrograph of a longitudinal section of Ti–20Y extruded at 800 °C to $\eta = 2.25$. Dark grey areas are Ti; light grey areas are Y.

composites. This is illustrated in Figs 2 and 3, where the microstructure is shown after the 800 °C extrusion to $\eta = 2.25$.

The size and spacing of the kinked, ribbon-shaped filaments decreased with continuing deformation up through $\eta = 7.27$, resulting in the nanofilamentary microstructure seen in Figs 4 and 5. At the highest levels of deformation ($\eta > 12$), the phases assume an equiaxed structure (Figs 6 and 7), presumably as a result of recrystallization during the many stress relief anneals performed on these specimens in the course of their cold drawing.

The pure Ti control specimen was coarse grained in the as-cast condition, and the initial deformation reduced the grain size approximately ten-fold. No grain size measurements were performed on the pure Ti control specimens at deformations greater than

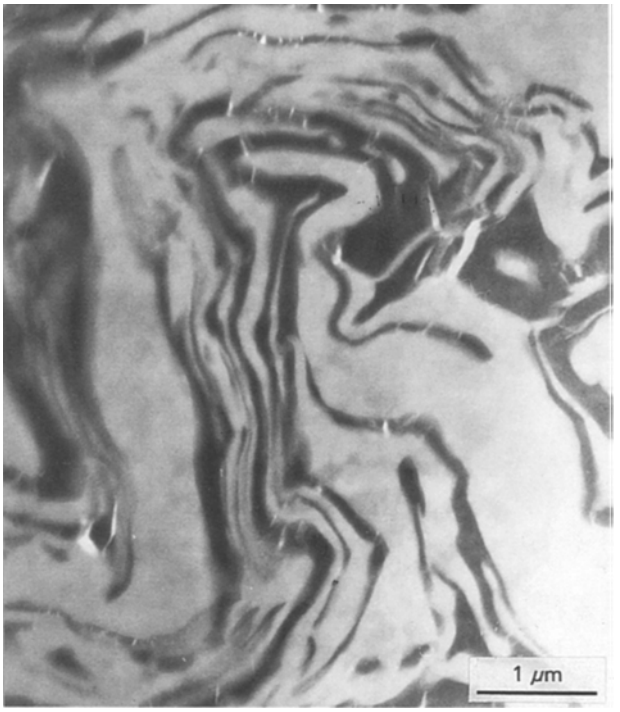

Figure 4 Conical scan dynamic dark field TEM micrograph of Ti–20Y deformation processed to $\eta = 5.03$ and sectioned transversely. The light grey areas are Ti, and the dark grey areas are Y. The Y phases display numerous fractures across their thickness. Note the similarity in phase shape to the Cu–20Nb specimen shown in Fig. 13.

Figure 5 Conical scan dynamic dark field TEM micrograph of Ti–20Y deformation processed to $\eta = 7.27$ and sectioned transversely.

$\eta = 5.03$. The phase size measurements are shown in Table I.

3.2. The effect of deformation on mechanical properties

As would be expected, deformation processing substantially increased the ultimate tensile strength (UTS) of both the Ti–20Y composite and of the pure Ti control specimen. Fig. 8 shows that the Ti–20Y composite more than tripled in UTS as η increased from 0 to 7.27, similar to the UTS increase seen in Cu–20Nb and in the Ti–20Y composite studied earlier [12] for similar η values. The maximum in this plot is seen at the highest deformation level where the kinked ribbon-shaped phases were observed. At greater values of

Figure 6 Bright field TEM micrograph of Ti–20Y deformation processed to $\eta = 12.2$, annealed at 700 °C, and sectioned transversely. Note the generally equiaxed grains and the lack of plane strain filamentary microstructure as compared to Figs 4 and 5.

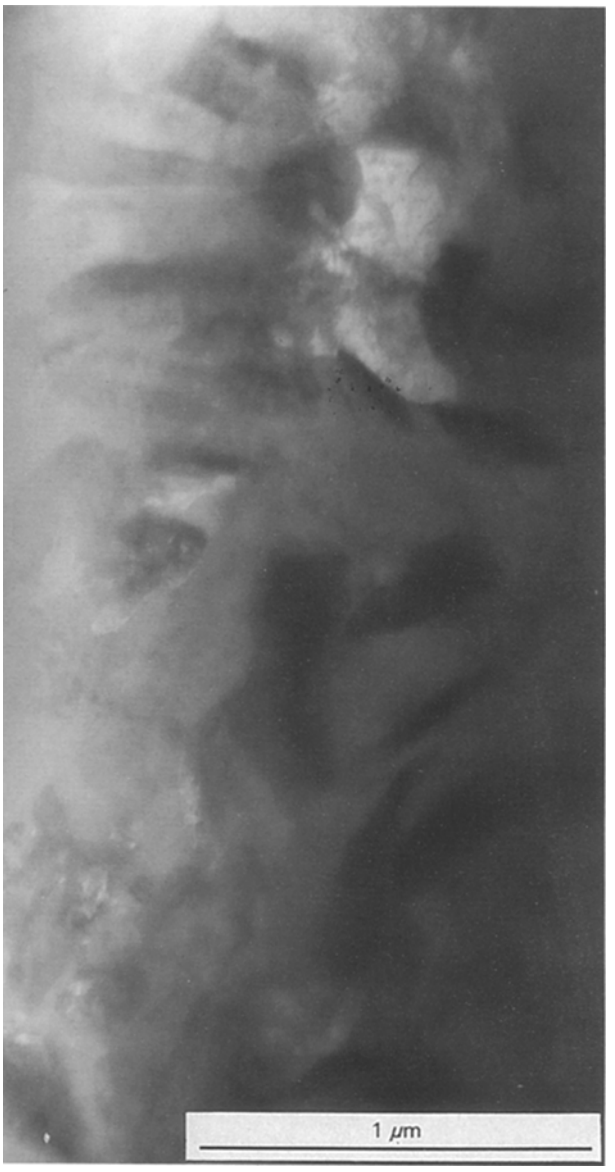

Figure 7 Conical scan dynamic dark field TEM micrograph of Ti–20Y deformation processed to $\eta = 12.8$ and sectioned transversely. This specimen was cold-worked to a 60% reduction in area by drawing with no subsequent anneal. Note incipient formation of chevron-patterned phase boundaries presumably caused by plane strain in the Ti and Y phases.

TABLE I Average phase sizes measured by optical microscopy, SEM and TEM for the Ti control and Ti–20Y

True strain (η)	Pure Ti average grain diameter (μm)	Ti–20Y average Ti phase thickness (μm)	Ti–20Y average Y phase thickness (μm)	Ti–20Y average phase diameter (μm)
0	760	9.6	2.4	
2.25	65	3.8	0.96	
5.03	70	0.69	0.17	
7.27		0.16	0.041	
12.2				0.23
12.8				0.20

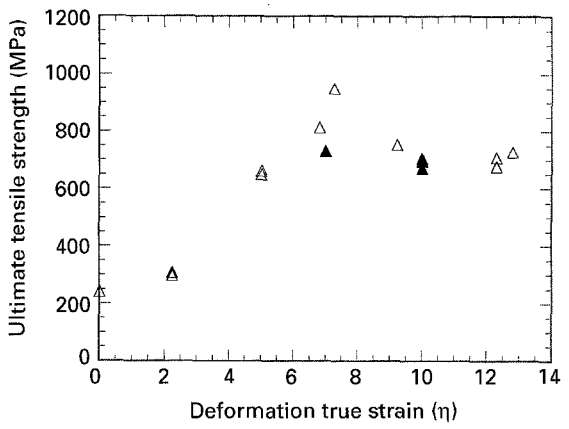

Figure 8 Ultimate tensile strength versus deformation processing of Ti–20Y composite by extrusion, swaging and wire drawing. △, Ti–20Y; ▲, Ti–20Y (2nd generation).

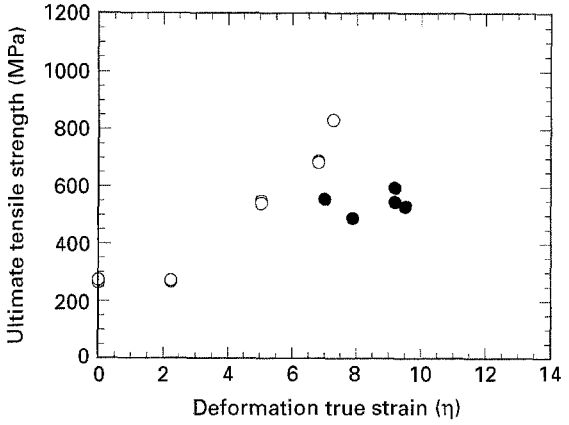

Figure 9 Ultimate tensile strength versus deformation processing of pure Ti by extrusion, swaging and wire drawing. ○, Pure Ti; ●, pure Ti (2nd generation).

η, the recrystallized phases were approximately equiaxed and strength decreased.

As shown in Fig. 9, the UTS of the pure Ti control specimen also increased with deformation processing, reaching its maximum at the same $\eta = 7.27$ level as the maximum of the Ti–20Y specimen. Ductility measurements of all specimens were consistently high, as shown in Table II.

3.3. Gas fusion analysis results

Oxygen and nitrogen have little effect on either strength or ductility in Y at the levels seen in these specimens [14]. However, O and N are powerful strengthening and embrittling agents in Ti [15], and for that reason the levels of these interstitial impurities were monitored by the gas fusion analysis results shown in Table III. The O and N increases observed in the specimens as a result of the deformation and annealing treatments are relatively modest. Over the range of values seen (ca. 450 wt p.p.m.), O increases the ultimate tensile strength in Ti by *ca.* 35 MPa [15]; and in Y the addition of 450 wt p.p.m. O would have no discernible effect on ultimate tensile strength [14]. Since 35 MPa is quite small compared to the amount of change observed in ultimate tensile strength during deformation processing, the effect of O content change was assumed to be a minor contributor to the observed changes in ultimate tensile strength.

TABLE II Ultimate tensile strength and ductility measurements for tensile specimens of Ti–20Y and pure Ti

Specimen	Ultimate tensile strength (MPa)	Ductility: reduction in area at fracture surface (%)
Ti–20Y as-cast ($\eta = 0$)	242	38
Ti–20Y as-cast ($\eta = 0$)	242	36
Ti–20Y as-extruded ($\eta = 2.25$)	307	47
Ti–20Y as-extruded ($\eta = 2.25$)	298	48
Ti–20Y ($\eta = 5.03$)	649	45
Ti–20Y ($\eta = 5.03$)	662	45
Ti–20Y ($\eta = 6.82$)	813	37
Second generation: Ti–20Y ($\eta = 7.0$)	731	52
Ti–20Y ($\eta = 7.27$)	949	42
Ti–20Y ($\eta = 9.24$)	753	45
Second generation: Ti–20Y ($\eta = 10.0$)	705	59
Second generation: Ti–20Y ($\eta = 10.0$)	671	63
Second generation: Ti–20Y ($\eta = 10.0$)	695	55
Ti–20Y ($\eta = 12.3$) (full anneal)	708	61
Ti–20Y ($\eta = 12.3$ (full anneal)	678	37
Ti–20Y ($\eta = 12.3$) (full anneal)	708	56
Ti–20Y ($\eta = 12.8$) (60% cold work)	727	11
Pure Ti as-cast ($\eta = 0$)	275	79
Pure Ti as-cast ($\eta = 0$)	265	76
Pure Ti as-extruded ($\eta = 2.25$)	272	88
Pure Ti as-extruded ($\eta = 2.25$)	268	88
Pure Ti ($\eta = 5.03$)	550	68
Pure Ti ($\eta = 5.03$)	542	70
Pure Ti ($\eta = 6.82$)	684	70
Pure Ti ($\eta = 6.82$)	690	68
Second generation: Pure Ti ($\eta = 7.00$)	557	84
Pure Ti ($\eta = 7.27$)	832	63
Second generation: Pure Ti ($\eta = 7.87$)	490	75
Second generation: Pure Ti ($\eta = 7.87$)	491	76
Second generation: Pure Ti ($\eta = 9.19$)	597	75
Second generation: Pure Ti ($\eta = 9.19$)	547	76
Second generation: Pure Ti ($\eta = 9.53$)	530	76

3.4. X-ray texture measurements

Pole figures for the as-cast Ti–20Y and pure Ti specimens showed no significant texture. After deformation

began, however, a strong $\langle 10\bar{1}0\rangle$ fibre texture was observed in both the pure Ti control specimen and in the Ti and Y phases of the Ti–20Y composite throughout the deformation processing range, $2.25 \leq \eta \leq 7.27$ (see Figs 10–12). The $\langle 10\bar{1}0\rangle$ fibre texture is normally observed in drawn Ti [16], and its occurrence in drawn Y has been less thoroughly studied [17], but seems a likely texture for Y since its $c{:}a$ ratio is identical to that of Ti.

4. Discussion

4.1. Texture induced plane strain in both matrix and second phase of Ti–20Y

In the Cu–X deformation processed composites (where X is a bcc transition metal second phase insoluble in Cu), the second phase typically forms a $\langle 1\,1\,0\rangle$ fibre texture, while the Cu matrix develops a $\langle 1\,1\,1\rangle$ fibre texture often accompanied by a $\langle 0\,0\,1\rangle$ fibre texture [18–21]. In a bcc crystal with a $\langle 1\,1\,0\rangle$ fibre texture, two of the four $\langle 1\,1\,1\rangle$ directions (the $[1\,\bar{1}\,1]$ and the $[\bar{1}\,\bar{1}\,1]$) are positioned perpendicular to the centre line and thus cannot slip. All slip is limited to the remaining two $\langle 1\,1\,1\rangle$ directions (the $[1\,1\,1]$ and the $[\bar{1}\,1\,1]$) which lie opposite one another across the specimen centre line, thus limiting the bcc phase to plane strain [1, 22]. The fcc Cu matrix, however, can readily deform axisymmetrically in either the $\langle 1\,1\,1\rangle$ or $\langle 0\,0\,1\rangle$ fibre texture, since these orientations possess three and four slip directions, respectively, to accommodate plastic flow. The Cu–X deformation processed composites are therefore characterized by plane straining bcc second phases embedded in a Cu matrix whose several active slip systems can accommodate the changing filament aspect ratios of the second phase.

The axisymmetrically deforming fcc Cu surrounding the plane straining bcc filaments constrains the X filaments and results in the curling and folding effect evident in Fig. 13. Thus, for an equivalent amount of deformation, Cu–X deformation processed composites have a much thinner effective filament thickness and a much larger interfacial area than do fcc–fcc deformation-processed composites like Ag–Cu or Ag–Ni. The deformation processed Ag–Cu wire of Frommeyer and Wassermann [23] was comprised of 100% fcc fibres which deform axisymmetrically, and these specimens achieved much lower maximum UTS values (1250–1400 MPa), even at filament thicknesses of only 12–25 nm. Bevk *et al.* [1] suggested that the presence of a plane straining phase is one of the reasons for the superior strength of the Cu–X composites.

TABLE III Gas fusion analysis results for Ti–20Y composite and pure Ti control specimens

Specimen	O Content (wt p.p.m.)	N Content (wt p.p.m.)
Ti–20Y as-cast ($\eta = 0$)	827	37
Ti–20Y as-extruded ($\eta = 2.25$)	895	42
Ti–20Y ($\eta = 6.68$)	817	43
Ti–20Y ($\eta = 12.3$)	663	46
Pure Ti as-cast ($\eta = 0$)	434	21
Pure Ti as-extruded ($\eta = 2.25$)	499	32
Pure Ti ($\eta = 6.68$)	731	41

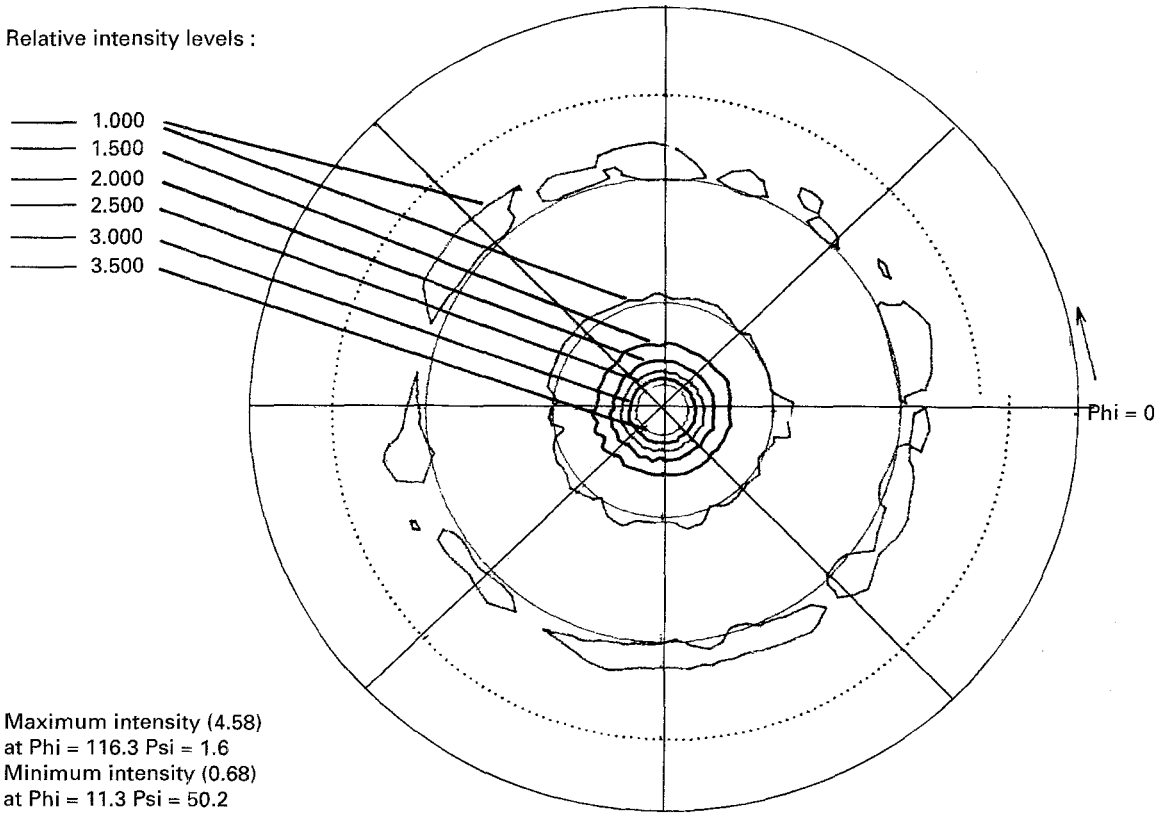

Figure 10 Pole figure for pure Ti deformation processed to $\eta = 5.03$ taken with X-rays diffracted from the $(01\bar{1}0)$ plane. An "ideally textured" Ti rod with a $\langle 10\bar{1}0\rangle$ fibre texture would display a central spot of high intensity and a ring at psi = 60° of moderate intensity.

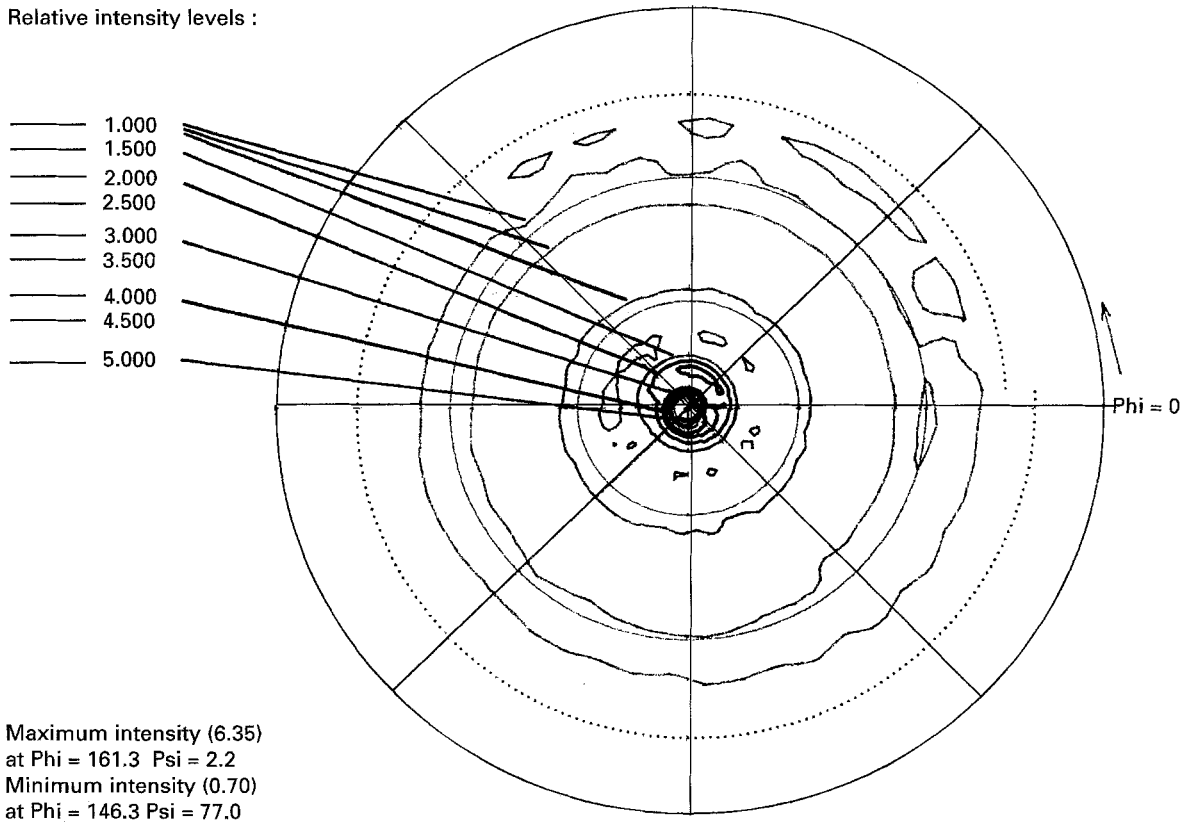

Figure 11 Ti $(1\,0\,\bar{1}\,0)$ pole figure for Ti–20Y ($\eta = 5.03$). An ideally textured specimen with a $\langle 1\,0\,\bar{1}\,0\rangle$ fibre texture would display a strong central spot and a less intense ring at psi = 60°.

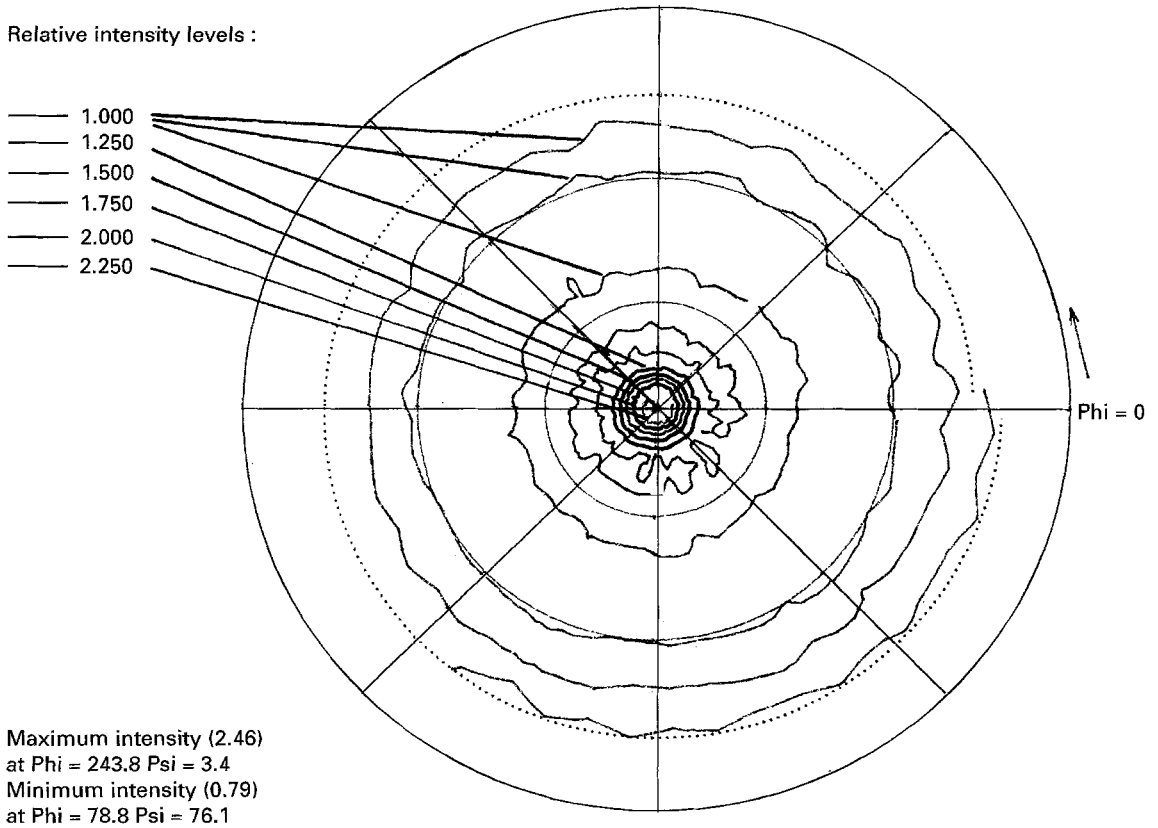

Figure 12 Y $(1\,0\,\bar{1}\,0)$ pole figure for Ti–20Y ($\eta = 5.03$). An ideally textured specimen with a $\langle 1\,0\,\bar{1}\,0\rangle$ fibre texture would display a strong central spot and a less intense ring at psi = 60°.

In the Ti–20Y deformation processed composite, the observed $\langle 1\,0\,\bar{1}\,0\rangle$ fibre texture in both the Ti and the Y limits both the Ti matrix and the Y second phase to plane strain. This results from the orientation of the two active slip systems in Ti (and presumably in Y as well) at room temperature. In a study of deformation mechanisms active in Ti, Anderson *et al.* [24] found that two slip systems are active in pure Ti at room

Figure 13 Conical scan dynamic dark field TEM micrograph of Cu–20Nb deformation processed to $\eta = 7$. The Cu matrix appears dark grey, and the Nb filaments appear light grey. Note the characteristic curling and folding of the Nb filaments necessary to accommodate their plane straining aspect ratio change within the axisymmetrically deforming Cu matrix.

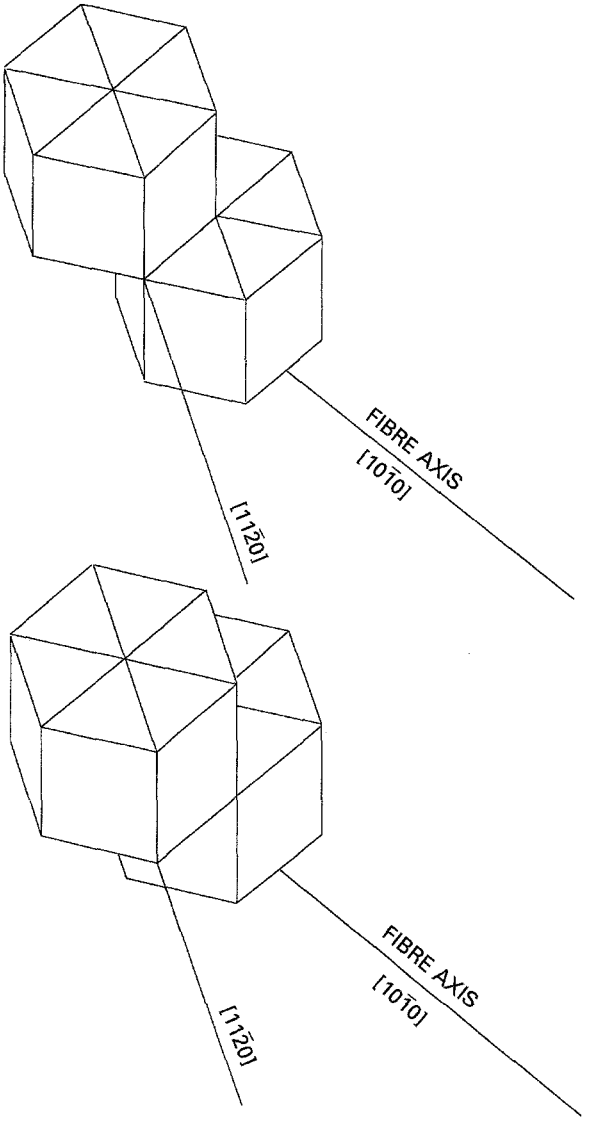

Figure 14 Illustration of the relative orientations of two hexagonal close-packed unit cells with a $\langle 1\,0\,\bar{1}\,0\rangle$ fibre texture before and after a slip of one Burger's vector magnitude on the $(0\,0\,0\,2)\,\langle 1\,1\,\bar{2}\,0\rangle$ slip system. This slip system has a resolved shear stress of zero in this orientation, and thus would be inactive in $\langle 1\,0\,\bar{1}\,0\rangle$ fibre textured metal.

temperature. The critical resolved shear stress (CRSS) for slip in the $\langle 1\,1\,\bar{2}\,0\rangle$ direction on the $(0\,0\,0\,2)$ basal plane (illustrated in Fig. 14) was found to be 110 MPa, and the CRSS for slip in the $\langle 1\,1\,\bar{2}\,0\rangle$ direction on the $\{1\,0\,\bar{1}\,0\}$ first order prism planes (illustrated in Fig. 15) was found to be 50 MPa.

With a CRSS of 110 MPa in the $(0\,0\,0\,2)\,\langle 1\,1\,\bar{2}\,0\rangle$ slip system in Ti, it is not surprising that Ti textures to optimize slip on the $\{1\,0\,\bar{1}\,0\}\langle 1\,1\,\bar{2}\,0\rangle$ slip system, where the CRSS is lower at 50 MPa. It seems likely that Y, with the same low $c{:}a$ ratio as Ti, behaves similarly. With the $\langle 1\,0\,\bar{1}\,0\rangle$ fibre texture observed for both Ti and Y in this experiment, applying Schmid's Law to calculate the shear stress for basal plane slip yields

$$\tau_r = \sigma \cos\phi \cos\lambda = 0$$

where τ_r is the resolved shear stress on the given slip system, σ the stress on the rod (force/cross-sectional area), λ the angle between the rod axis and the slip direction (30° or 90°), and $\phi =$ the angle between the rod axis and the normal to the slip plane (90°). Thus, basal slip would not occur in a $\langle 1\,0\,\bar{1}\,0\rangle$ fibre textured rod.

If Schmid's Law is applied to the $\{1\,0\,\bar{1}\,0\}\langle 1\,1\,\bar{2}\,0\rangle$ slip system in a rod with the $\langle 1\,0\,\bar{1}\,0\rangle$ fibre texture, λ becomes 30° and ϕ becomes 60°, which yields a resolved shear stress of

$$\tau_r = \sigma \cos\phi \cos\lambda = \sigma \cos(60°)\cos(30°) = 0.433\sigma$$

A resolved shear stress of 0.433σ is near the maximum possible value of 0.5σ, and this slip system must be the active one in axisymmetrically deformed specimens with the $\langle 1\,0\,\bar{1}\,0\rangle$ fibre texture.

There is a striking similarity between the arrangement of available slip systems in a hexagonal close-packed lattice with the $\langle 1\,0\,\bar{1}\,0\rangle$ fibre texture and the bcc lattice with the $\langle 1\,1\,0\rangle$ fibre texture. Both situations limit slip to two directions that are opposite one another across the rod centre line (as compared with the three or four slip directions possible in a fcc lattice), and both would be expected to result in plane strain of each individual phase within the composite specimen. Thus, this analysis would predict that a deformation-processed composite comprised of hexagonal close-packed metals would undergo the same filament shaping processes that have been observed in the bcc filaments of Cu–X composites. Since both the Ti and the Y are limited to plane strain in the $\langle 1\,0\,\bar{1}\,0\rangle$ fibre texture orientation, the twisted ribbon shape so

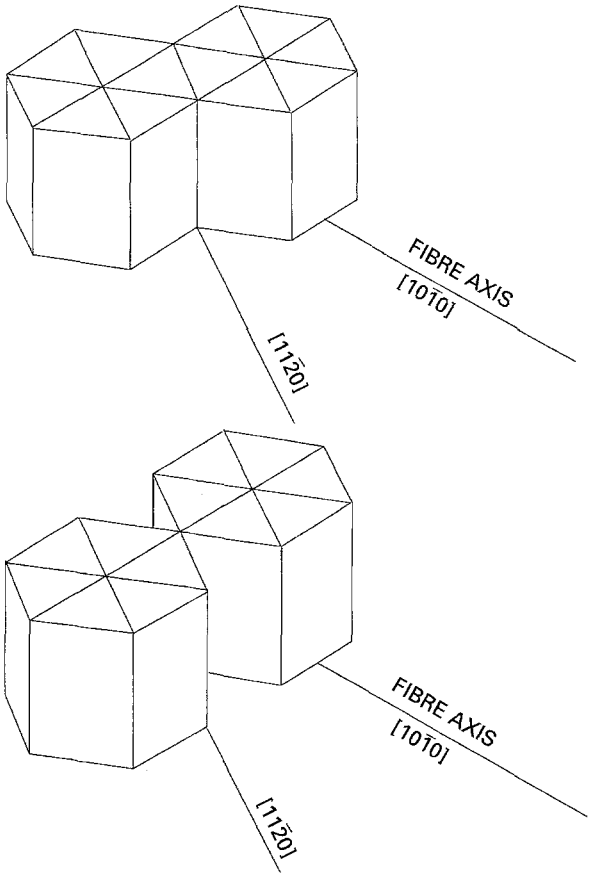

Figure 15 Illustration of the relative orientations of two hexagonal close-packed unit cells with a $\langle 1\,0\,\bar{1}\,0\rangle$ fibre texture before and after a slip of one Burger's vector magnitude on the $\{1\,0\,\bar{1}\,0\}\langle 1\,1\,\bar{2}\,0\rangle$ slip system.

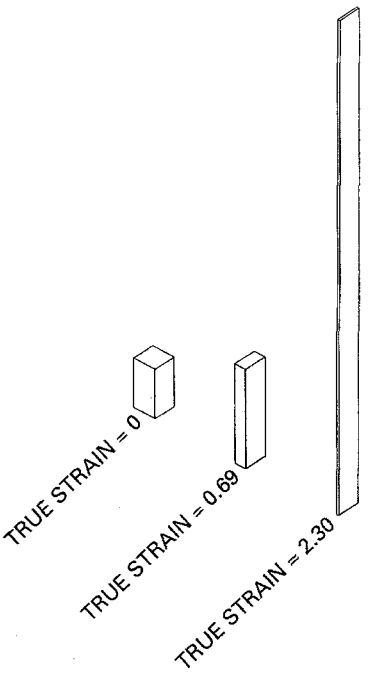

Figure 16 Aspect ratio changes in a $1 \times 1 \times 2$ rectangular prism deforming by plane strains of 0.69 and 2.30.

frequently seen in the bcc filaments of Cu–X composites would be expected for all phases in the Ti–Y composite. The very thin filaments with exceptionally large interfacial boundary area inherent in such phase morphology might in turn produce the anomalous strengthening observed with the fcc–bcc Cu–X composites but absent in the fcc–fcc composites such as Ag–Cu [23]. Indeed, the increase in strength observed for the Ti–20Y composite in Fig. 8 is quite similar to that observed in the Cu–20Nb composites [1,4] over the range $0 \leq \eta \leq 7.27$. At $\eta > 7.27$, the Ti–20Y composites recrystallized at higher annealing temperatures or broke apart when lower annealing temperatures were employed, preventing the higher η value comparison between Cu–X and Ti–Y composites which would be of greatest interest.

4.2. Geometrical factors in the inability of Ti–20Y to tolerate large deformations

Throughout the various deformation processing operations performed on the Ti–20Y composite after its hot extrusion to $\eta = 2.25$, this composite was never cold worked to an additional true strain > 5.02 without either recrystallizing during recovery anneals or breaking. This same behaviour was also observed with earlier experiments performed on smaller castings of Ti–20Y and Ti–50Y [12]. This suggests that some fundamental difference exists between the Cu–X composites (which have undergone true strains as large as 13 before breaking) and the Ti–20Y composite.

One possible explanation for this difference in behaviour is the geometric difficulty of fitting a material comprised of 100% plane straining phases within a cylinder of diminishing radius. Fig. 16 depicts the extensive shape change that would result from deforming a rectangular prism with initial dimensions of $1 \times 1 \times 2$ units (roughly equivalent to the Ti dendrite aspect ratio in Ti–20Y as can be seen in Fig. 1) through plane strains of 0.69 and 2.30. Note that the prism elongates in the vertical dimension and narrows in one, the $\langle 1\,1\,\bar{2}\,0\rangle$, of the two transverse dimensions while the other transverse dimension, the $\langle 0\,0\,0\,1\rangle$, remains unchanged. Assuming no volume change during this deformation, the prism deformed by plane strain to $\eta = 2.30$ increases 10-fold in height while decreasing 10-fold in thickness. Although not shown on Fig. 16, a further deformation by plane strain to a total strain of $\eta = 5$ would result in a prism with a height of nearly 300 units and a thickness of 0.0067 units. Fitting many such plane straining ribbons into an overall cylindrical specimen shape is not a simple task. A valid mathematical determination of a geometrical limit of η for such a situation is unquestionably a formidable problem and may be so complex as to be beyond the "state of the art" of current foliation theory; however, qualitative consideration of some of the possible geometric arrangements to accommodate such deformation is possible and is presented here.

The upper portion of Fig. 17 shows a transverse section of a "tiled" array of polygons representing Ti and Y in an arrangement of 80% by volume Ti and 20% by volume Y, which is roughly equivalent to the geometry of the as-cast dendrites observed in Fig. 1. The lower portion of Fig. 17 depicts one possible geometry for the deformation by the plane strain to

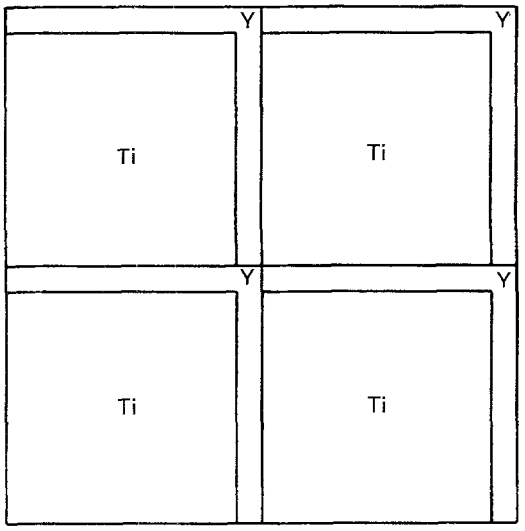

TRUE STRAIN = 0
AS - CAST DENDRITES

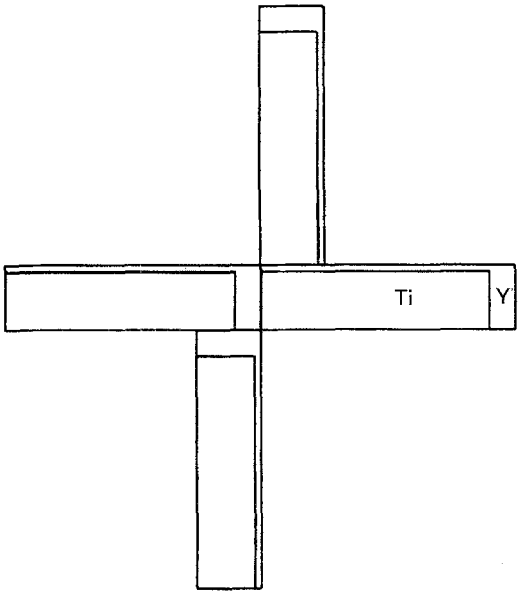

TRUE STRAIN = 1.39
CRUCIFORM ARRAY

Figure 17 Possible tiling arrays for as-cast (above) and $\eta = 1.39$ (below) Ti–20Y.

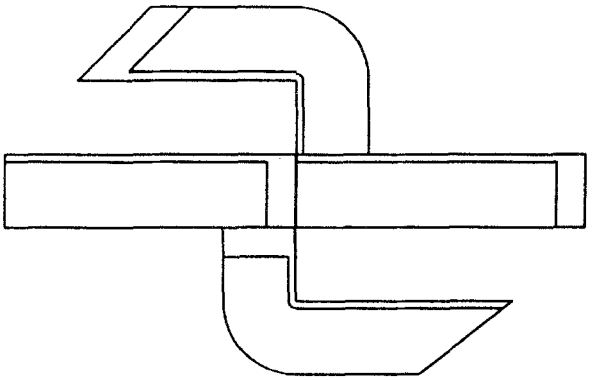

TRUE STRAIN = 1.39
CRUCIFORM ARRAY WITH
PARTIAL PINWHEEL BENDING

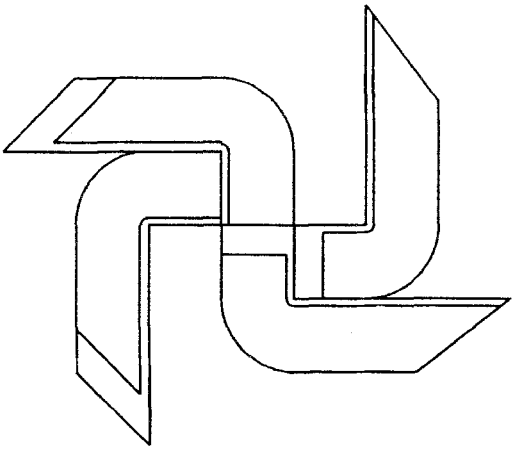

TRUE STRAIN = 1.39
CRUCIFORM ARRAY WITH
PINWHEEL BENDING

Figure 18 Two modifications of the cruciform array in Fig. 17 by basal plane (0 0 0 2) slip bending of the Ti and Y phases.

$\eta = 1.39$ of the "as-cast" polygons. The cruciform array resulting from this deformation is consistent with a plane strain mode of deformation in both the Ti and Y phases, but such a cruciform array allows no contiguous, void-free tiling with neighbouring phases also possessing such a cruciform arrangement.

Fig. 18 depicts two possible modifications to the transverse section view of the simple cruciform array in Fig. 17 that permit the arrays to achieve better compatibility with their neighbours. Both Ti and Y textured with the $\langle 1\,0\,\bar{1}\,0 \rangle$ fibre texture can bend by slip on the basal (0 0 0 2) plane (see Fig. 14) to achieve the shapes in Fig. 18, and in so doing they develop tile shapes which can more nearly fit in a contiguous, void-free arrangement with neighbouring arrays, as shown in Fig. 19. Figs 20 and 21 depict an alternative to the cruciform array in which the polygons are arranged parallel to the specimen's outer circumference in a pattern similar to the annual growth rings of a tree trunk. Such an arrangement provides a nearly perfect contiguous, void-free array with neighbouring tiles; however, it allows for no reduction in the circumference of the array as the specimen size is further reduced by more deformation processing since it positions the dimension which is unchanging in plane strain parallel to the specimen's circumference. A possible accommodation to this problem is shown in Fig. 21, where the polygons bend by slip on the Ti and Y basal (0 0 0 2) planes to accommodate the diminishing circumference caused by further deformation processing. Such bowing of the polygons, however, will be only temporarily adequate to accommodate

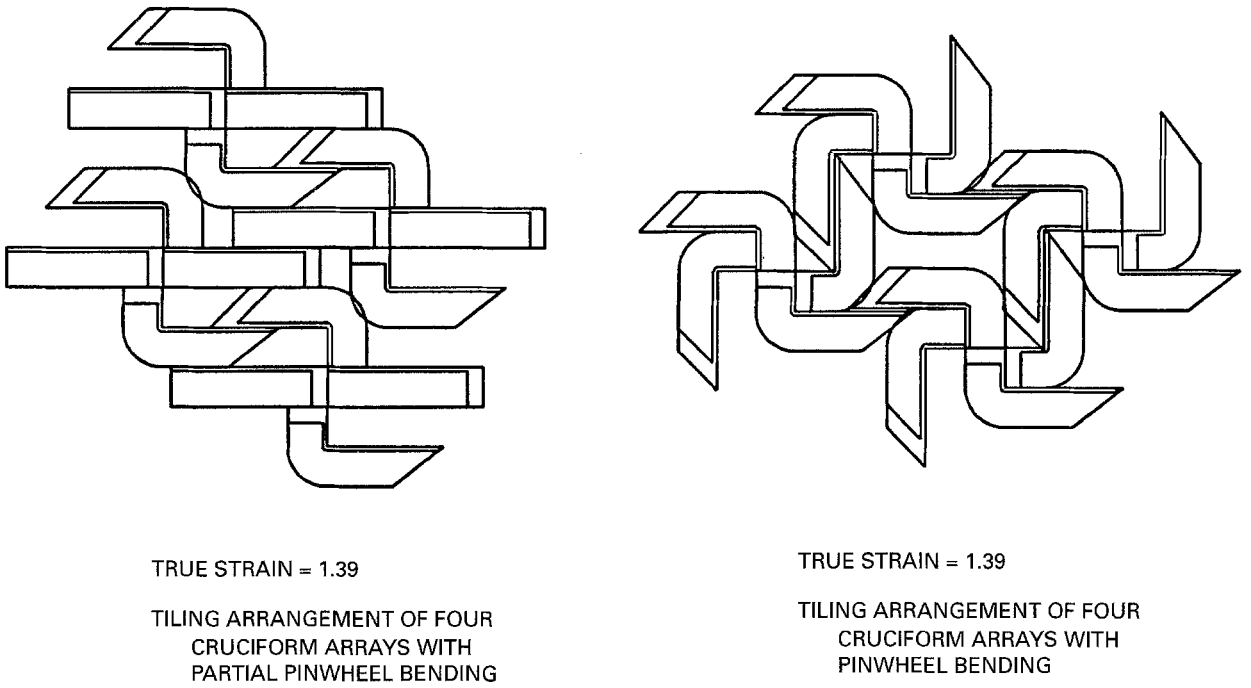

Figure 19 Two possible tiling arrangements of the modified cruciform arrays shown in Fig. 18 that more nearly fill the available area in a contiguous, void-free tiling.

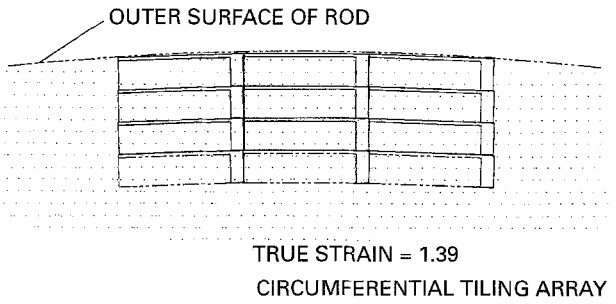

Figure 20 A possible circumferential ("tree ring") tiling arrangement of Ti–20Y deformed by plane strain to $\eta = 1.39$ where the phases bend slightly by basal slip (0002) to conform to the cylindrical contours of the specimen.

continuing deformation, since it repositions the polygons in an orientation that does not permit the radius to diminish with still further deformation processing.

The true strain of 1.39 depicted in Figs 17–21 corresponds to a 4:1 reduction ratio by plane strain. Although none of the suggested arrangements offers an ideal accommodation to the plane strain space-filling problem, one can assume that some combination of these various arrays could accommodate the need for both the Ti and the Y to flow by plane strain. The space-filling challenge becomes more severe, however, when one contemplates the 16:1 reduction ratio of $\eta = 2.77$ true strain depicted in Fig. 22. Here the large aspect ratio of the polygons magnifies the difficulties in fitting these polygons into the confines of a cylindrical specimen shape. The cruciform array shown in Fig. 22 is substantially more difficult to modify by pinwheel bending schemes into any possible arrangement that maintains a contiguous, void-free match with neighbouring arrays without necessitating inordinate amounts of grain boundary sliding. The only apparent means to accommodate the diminishing radius and circumference of the specimen is to employ circumferential "tree ring" tiling schemes with more than one bend, rather like the convoluted bending patterns seen in Fig. 4 of Ti–20Y cold-worked an additional $\eta = 2.78$ after hot extrusion. Even at that, the Y filaments in Fig. 4 can be seen to contain numerous fractures (visible as narrow white cracks across the Y filaments) where the accommodation stresses exceeded the Y fracture strength.

It should be noted that all the hypothetical tiling arrays discussed here are predicated on the assumptions that the phases possess ideal $\langle 10\bar{1}0\rangle$ fibre texture and that only the $\{10\bar{1}0\}\langle 11\bar{2}0\rangle$ slip system is operating to permit elongation of the specimens. Indeed, deviations from those assumptions are probably responsible for the success in cold working the Ti–20Y composite to true strains as high as $\eta = 7.27$. One must also bear in mind that all the tiling schemes discussed here are indistinguishable from one another by X-ray texture analysis on transverse sections, and thus only phase shapes from the micrographs can be used to judge how nearly the various tiling schemes match the actual deformation pattern of the composite.

The preceding discussion suggests that it may be difficult to extrude, swage, or draw any metal–metal matrix composite to very high η values in the absence of at least one "accommodating" phase like the fcc Cu in Cu–X that has a sufficient number of active slip systems to avoid these plane strain geometric fitting limitations. Thus, most of the possible deformation processed composites consisting of immiscible hcp–hcp, hcp–bcc or bcc–bcc combinations may be rather stringently limited in their maximum attainable η values. Since most metallic elements are not fcc, such a conclusion suggests a major limitation to

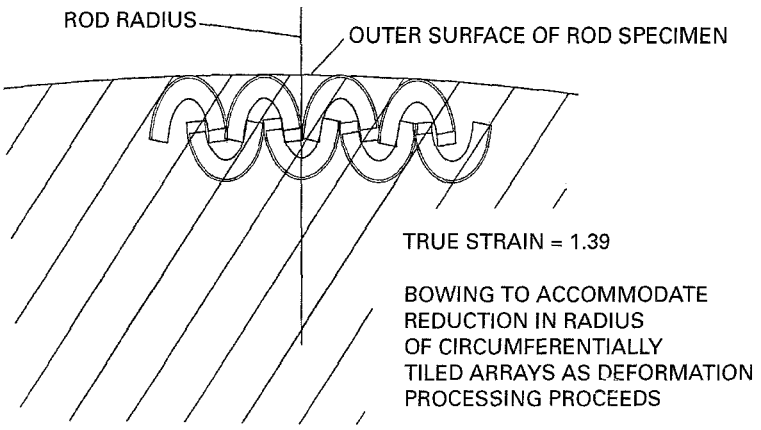

Figure 21 Depiction of "bowing" by basal plane slip (0 0 0 2) of the Ti and Y phases to accommodate further deformation of the "tree ring" tiling arrangement as the specimen radius (and circumference) diminish with continuing deformation processing by drawing.

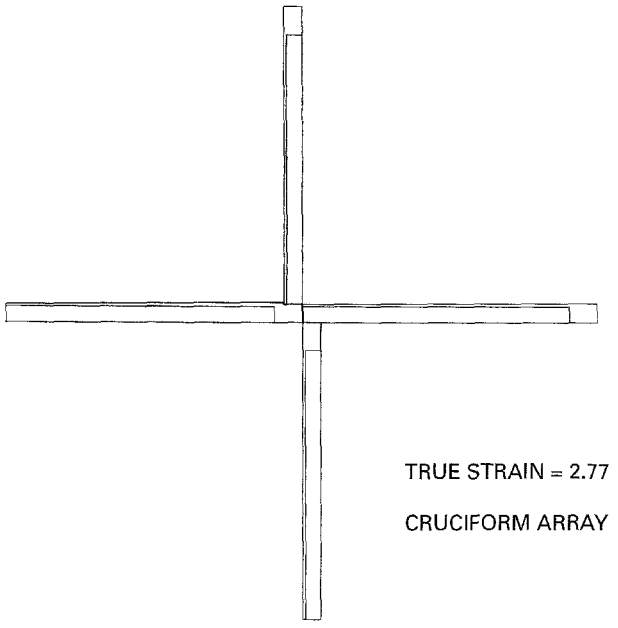

Figure 22 Pinwheel array of Ti–20Y polygons deformed to $\eta = 2.77$.

the prospective engineering applications of deformation processing to commercially useful alloy systems.

There are, however, still means available to produce deformation processed composites without fcc phases, including the following:

1. By starting the deformation processing with a specimen possessing exceptionally fine dendrites (by casting with melt spinning or similar techniques) or powder particle sizes (by mechanical alloying, CIP and/or HIP processing), one might achieve a filamentary microstructure in the range of tens of nanometres after deformation processing to relatively modest true strains.
2. By deformation processing hcp or bcc matrix composites at carefully selected elevated temperatures, one might be able to avoid recrystallization and coarsening while benefitting from the additional slip systems (to permit axisymmetric strain rather than plane strain) which become active at elevated temperatures. This strategy may be particularly effective in bcc metals, where alternative slip systems are available with only modestly higher resolved shear stresses.
3. Deformation processing by rolling the composite into sheet rather than swaging or drawing the composite into rod/wire forms would presumably avoid the geometric constraint of fitting plane straining phases into a cylindrical specimen shape. In rolled sheet, both the Ti and Y phases would be free to assume the natural lamellar shape that results from plane strain.

The commercial ramifications of the third item above are potentially large. Plate and sheet products are more useful in most engineering applications than rod or wire. If Ti and Y in a Ti–20Y composite acquire the rolling texture typically seen in pure Ti, they would form lamellae with the crystallographic alignment depicted in Fig. 23. In this arrangement, the $\langle 10\bar{1}0 \rangle$ axis of the crystal aligns with the rolling direction and the $\langle 0001 \rangle$ direction is tilted at a 20–40° angle to the sheet normal [29]. Such a texture would position the lamellae with their $\langle 11\bar{2}0 \rangle$ slip directions tilted 20°–40° with respect to the lamellae boundaries. Thus, a dislocation on the only available slip direction for either basal or prism slip could move only a relatively limited distance before encountering the next lamella in the sheet. This is in contrast to the situation in Cu–X sheet where the large number of available slip directions in the fcc matrix permit some dislocations to run very large distances before encountering a lamellar barrier and where the strengths of sheet are much lower than the strengths of wire.

Overall, this study suggests that the prospect for producing rod or wire product of Ti–20Y by room temperature deformation processing of conventionally cast material appear to be limited at best. However, the potential exists to develop useful Ti–20Y (and possibly other hcp–hcp, hcp–bcc or bcc–bcc) composites in plate/sheet form where the plane strain limitation of the deforming phases could be an asset to achieving high strength in a composite with the excellent interphase bonding afforded by two metallic phases.

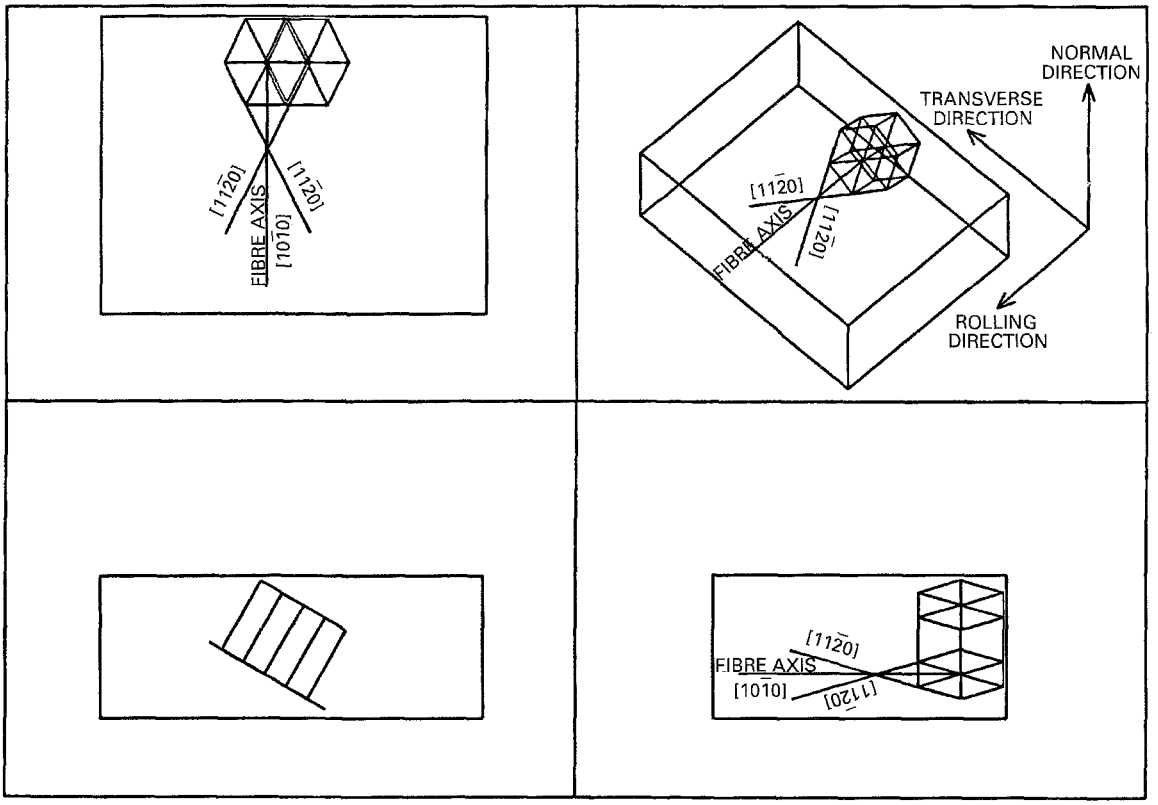

Figure 23 Top, front, right profile, and isometric views of the crystallographic texture of a rolled Ti or Y lamella with the $\langle 10\bar{1}0 \rangle$ direction parallel to the rolling direction and the $\langle 0001 \rangle$ direction tilted at 20–40° from the rolled sheet normal.

Acknowledgements

The authors are grateful to J. D. Verhoeven, R. K. Trivedi, L. L. Jones, L. P. Lincoln, L. K. Reed and J. T. Wheelock, all of Ames Laboratory, for their valuable discussions and for preparing the materials used in this study. This work was performed at Ames Laboratory, operated for the US Department of Energy by Iowa State University under contract no. W-7405-ENG-82 and at G & S Titanium, Wooster, OH. Costs of the deformation processing were partially supported by Rohr, Inc. with additional financial support from the US Department of Energy and the Engineering Research Institute of Iowa State University.

The materials and processes described in this article are protected by US Patent 5 200 004 and other patents pending. Licensing inquiries should be directed to Mr John Weis, Office of Technology Commercialization, 151 ASC II, Iowa State University, Ames, IA 50011, USA.

References

1. J. BEVK, J. P. HARBISON and J. L. BELL, *Appl. Phys.* **49** (1978) 6031.
2. J. D. VERHOEVEN, F. A. SCHMIDT, E. D. GIBSON and W. A. SPITZIG, *J. Metals* **38** (1986) 20.
3. J. D. VERHOEVEN, W. A. SPITZIG, L. L. JONES, H. L. DOWNING, C. L. TRYBUS, E. D. GIBSON, L. S. CHUMBLEY, L. G. FRITZMEIER and G. D. SCHNITTGRUND, *J. Mater. Engng.* **12** (1990) 127.
4. W. A. SPITZIG and P. D. KROTZ, *Acta Metall.* **36** (1988) 1709.
5. J. D. VERHOEVEN, W. A. SPITZIG, F. A. SCHMIDT and C. L. TRYBUS, *Mater. Manufact. Proc.* **4** (1989) 197.
6. J. D. VERHOEVEN, W. A. SPITZIG, F. A. SCHMIDT, P. D. KROTZ and E. D. GIBSON, *J. Mater. Sci.* **24** (1989) 1015.
7. P. D. FUNKENBUSCH and T. H. COURTNEY, *Acta Metall.* **33** (1985) 913.
8. L. S. CHUMBLEY, H. L. DOWNING, W. A. SPITZIG and J. D. VERHOEVEN, *Mater. Sci. Engng.* **A117** (1989) 59.
9. C. L. TRYBUS, L. S. CHUMBLEY, W. A. SPITZIG and J. D. VERHOEVEN, *Ultramicroscopy* **30** (1989) 315.
10. P. D. FUNKENBUSCH and T. H. COURTNEY, *Scripta Metall.* **23** (1989) 1719.
11. W. A. SPITZIG, J. D. VERHOEVEN, C. L. TRYBUS, and L. S. CHUMBLEY, *Scripta Metall. Mater.* **24** (1990) 1171.
12. A. M. RUSSELL, T. W. ELLIS and L. S. CHUMBLEY, *J. Mater. Sci.* **30** (1995) p. 2070
13. E. E. UNDERWOOD, "Quantitative stereology" (Addison-Wesley, Mass., USA, 1970) Ch. 3 and 4.
14. O. N. CARLSON, D. W. BARE, E. D. GIBSON and F. A. SCHMIDT, in *Symposium on Newer Metals: Special Technical Publication No. 272* (American Society for Testing Materials, Philadelphia, USA, 1959) p. 144.
15. M. J. DONACHIE, Jr, "Titanium: A technical guide" (ASM International, Metals Park, Ohio, USA, 1988) p. 40.
16. B. W. CHRIST, *ASM Metals Handbook*, **8** (1985) 28.
17. A. I. PIKALOV, V. V. VOROB'YEV, I. I. PAPIROV and A. S. KAPCHERIN, *Izv. Akad. Nauk SSSR, Metally* **4** (1983) 153.
18. A. R. PELTON, F. C. LAABS, W. A. SPITZIG and C. C. CHENG, *Ultramicroscopy* **22** (1987) 251.
19. J. D. VERHOEVEN, W. A. SPITZIG, L. L. JONES, H. L. DOWNING, C. L. TRYBUS, E. D. GIBSON, L. S. CHUMBLEY, L. G. FRITZMEIER and G. D. SCHNITTGRUND, *J. Mater. Engng.* **12** (1990) 127.
20. C. A. TRYBUS, PhD thesis Iowa State University, USA (1988).
21. D. G. MORRIS and M. A. MORRIS, *Acta Metall. Mater.* **39** (1991) 1763.
22. W. F. HOSFORD, Jr, *Trans. Met. Soc. AIME* **230** (1964) 12.
23. G. FROMMEYER and G. WASSERMANN, *Acta Metall.* **23** (1975) 1353.
24. E. A. ANDERSON, D. C. JILLSON and S. R. DUNBAR, *J. Metals Trans AIME* **197** (1953) 1191.
25. G. Y. CHIN, *ASM Metals Handbook* **8** (1985) 229.

Received 14 November 1994
and accepted 15 March 1995